materials

MDPI

Communication

Tunable Pseudo-Piezoelectric Effect in Doped Calcium Titanate for Bone Tissue Engineering

Abdullah Riaz [1,*], Kerstin Witte [2], Wiktor Bodnar [2], Hermann Seitz [1,3], Norbert Schell [4], Armin Springer [5] and Eberhard Burkel [6]

1 Chair of Microfluidics, Faculty of Mechanical Engineering and Marine Technology, University of Rostock, Justus-von-Liebig-Weg 6, 18059 Rostock, Germany; hermann.seitz@uni-rostock.de
2 INP Leibniz Institute for Plasma Science and Technology, Felix-Hausdorff-Str. 2, 17489 Greifswald, Germany; kerstin.witte@inp-greifswald.de (K.W.); wiktor.bodnar@inp-greifswald.de (W.B.)
3 Department of Life, Light and Matter, University of Rostock, Albert Einstein-Str. 25, 18059 Rostock, Germany
4 Helmholtz-Zentrum Geesthacht, Max Plank-Str. 1, 21502 Geesthacht, Germany; norbert.schell@hzg.de
5 Medical Biology and Electron Microscopy Centre, University Medical Center Rostock, Strempel-Str. 14, 18057 Rostock, Germany; armin.springer@med.uni-rostock.de
6 Institute of Physics, University of Rostock, Albert Einstein-Str. 23-24, 18059 Rostock, Germany; eberhard.burkel@uni-rostock.de
* Correspondence: abdullah.riaz@uni-rostock.de; Tel.: +49-381-498-9138

Abstract: $CaTiO_3$ is a promising candidate as a pseudo-piezoelectric scaffold material for bone implantation. In this study, pure and magnesium/iron doped $CaTiO_3$ are synthesized by sol-gel method and spark plasma sintering. Energy dispersive X-ray mapping confirm the homogenous distribution of doping elements in sintered samples. High-energy X-ray diffraction investigations reveal that doping of nanostructured $CaTiO_3$ increased the strain and defects in the structure of $CaTiO_3$ compared to the pure one. This led to a stronger pseudo-piezoelectric effect in the doped samples. The charge produced in magnesium doped $CaTiO_3$ due to the direct piezoelectric effect is (2.9 ± 0.1) pC which was larger than the one produced in pure $CaTiO_3$ (2.1 ± 0.3) pC, whereas the maximum charge was generated by iron doped $CaTiO_3$ with (3.6 ± 0.2) pC. Therefore, the pseudo-piezoelectric behavior can be tuned by doping. This tuning of pseudo-piezoelectric response provides the possibility to systematically study the bone response using different piezoelectric strengths and possibly adjust for bone tissue engineering.

Keywords: $CaTiO_3$; doping; piezoelectric effect; X-ray diffraction; nanostructure; bone tissue engineering

Citation: Riaz, A.; Witte, K.; Bodnar, W.; Seitz, H.; Schell, N.; Springer, A.; Burkel, E. Tunable Pseudo-Piezoelectric Effect in Doped Calcium Titanate for Bone Tissue Engineering. *Materials* **2021**, *14*, 1495. https://doi.org/10.3390/ma14061495

Academic Editor: Andrea Spagnoli

Received: 27 January 2021
Accepted: 16 March 2021
Published: 18 March 2021

1. Introduction

It is well known that the human bone exhibits significant electrical activity for its growth and healing process [1,2]. Piezoelectric ceramics allow for the delivery of an electrical stimulus without the need for an external power source for biomedical applications [3]. Therefore, as for scaffolds in tissue engineering, there is an increasing interest in piezoelectric ceramics because of their potential for providing electrical stimulation to cells promoting tissue repair [3–5].

Piezoelectric ceramics used in medical applications such as bone tissue engineering have to be non-cytotoxic, whereas most common ceramics like zirconate titanate, lead titanate or their compounds with piezoelectric properties are harmful for humans upon their ion dissolution in biological fluids [6,7]. In contrast, perovskite calcium titanate ($CaTiO_3$) ceramic is a non-cytotoxic compound. It was inadvertently found that non-piezoelectric $CaTiO_3$ formed at the interface between hydroxyapatite (HA) and titanium implants during a coating procedure. This formation of $CaTiO_3$ on titanium-coated HA increased the osteoblast adhesion [8]. Studies also show that the bone binding strength is improved due to the modification of titanium surface with $CaTiO_3$ [9,10]. It could be

possible that $CaTiO_3$ can even lead to better results if it shows piezoelectric behavior. Recently, it was reported that distorted structure of spark plasma sintered $CaTiO_3$ showed pseudo-piezoelectric behavior which most likely was generated by local instability (due to defects like oxygen vacancies) of the normal TiO_6 octahedra [11]. Since the strength of piezoelectric effect can play an important role for triggering the bone cells in a healing process, there is a need to tune the pseudo-piezoelectric behavior of $CaTiO_3$. This tuning of pseudo-piezoelectric response is necessary to systematically study the bone response using different piezoelectric strengths.

It should be possible to increase or tune the pseudo-piezoelectric behavior of $CaTiO_3$ through slightly changing the crystal structure of $CaTiO_3$ by doping [12]. Consequently, the pseudo-piezoelectric behavior can be tuned in a way that the bone cells can sense stimulations to improve the healing process. Utilizing doping elements which are already present in human body, i.e., Mg and Fe, should not cause any harm [13,14]. In the present study, pure $CaTiO_3$ and doping with Mg and Fe were prepared and the effect of doping on the crystal structure and pseudo-piezoelectric behavior of $CaTiO_3$ was investigated.

2. Materials and Methods

The pure, Mg and Fe doped $CaTiO_3$ powders were prepared by sol-gel synthesis [15]. Calcium nitrate tetrahydrate ($Ca(NO_3)_2{\cdot}4H_2O$) powder (Chemsolute/Th. Geyer GmbH and Co. KG, Renningen, Germany), Magnesium nitrate hexahydrate ($Mg(NO_3)_2{\cdot}6H_2O$) and iron(III) nitrate nonahydrate ($Fe(NO_3)_3{\cdot}9H_2O$) powders (Alfa Aesar, Kandel, Germany), and titanium isopropoxide ($Ti(OC_3H_7)_4$) (Sigma-Aldrich/Merck KGaA, Darmstadt, Germany) were used as precursors. The powders were prepared with the molar ratios of 1:1 of Ca:Ti and 9:10:1 of Ca:Ti:Fe/Mg, for pure and doped $CaTiO_3$, respectively. Firstly, to prepare pure $CaTiO_3$, $Ca(NO_3)_2{\cdot}4H_2O$ and $Ti(OC_3H_7)_4$ were dissolved separately in ethanol and then $Ca(NO_3)_2{\cdot}4H_2O$ was mixed drop wise in $Ti(OC_3H_7)_4$ solution. Afterwards, the solution was stirred for 24 h at room temperature. Secondly, to synthesize doped powders, $Ca(NO_3)_2{\cdot}4H_2O$ along with ($Mg(NO_3)_2{\cdot}6H_2O$)/($Fe(NO_3)_3.9H_2O$) was mixed drop-wise in $Ti(OC_3H_7)_4$ solution. These solutions were also stirred for 24 h at room temperature. The resulting solutions were dried separately with a mini spray dryer (Büchi Labortechnik AG, Essen, Germany) and also in an oven (Nabertherm GmbH, Lilienthal, Germany) at 180 °C for 2 h. Subsequently, the powders were calcined in an oven at 650 °C in air.

The calcined powders were densified using the HP D5 Spark Plasma Sintering (SPS) unit (FCT Systeme GmbH, Rauenstein, Germany) located in the Tycho Sinterlab, University of Rostock, Germany. The sintering of pure and doped powders was performed in vacuum of approximately 1 mbar. The applied load was adjusted to a value of 6 kN, resulting in a pressure of approximately 76 MPa inside of the die. The powders were heated up to 1025 °C (pure $CaTiO_3$), 975 °C (Mg doped) and 925 °C (Fe doped) with a heating rate of 100 K/min. The samples were sintered for 5 min at elevated temperatures and afterwards cooled down naturally. To adjust the height of the pure and doped samples for further experiments, a diamond band saw was used to precisely cut the samples. The final dimensions of all samples were 10 mm × 2 mm (diameter × height).

For elemental mapping, samples were mounted on Al-SEM-carrier with adhesive conductive carbon tape (co. PLANO, Wetzlar, Germany) and coated with carbon under vacuum (EM SCD 500, Co. Leica, Bensheim, Germany). Afterwards, samples were analyzed by a field emission scanning electron microscope (SEM, MERLIN® VP Compact, Co. Zeiss, Oberkochen, Germany) equipped with an energy dispersive X-ray (EDX) detector (XFlash 6/30, Co. Bruker, Berlin, Germany). A representative area (218.1 µm × 158.1 µm) of the samples were analyzed (for quantification: 500,000 counts were recorded) and mapped for elemental distribution on basis of the EDX-spectra data by QUANTAX ESPRIT v.2.0. (Co. Bruker, Berlin, Germany) Microanalysis software.

High Energy X-ray Diffraction (HEXRD) experiments were carried out at the High Energy Material Science (HEMS) beamline P07b located at high brilliance synchrotron radiation storage ring PETRA III, DESY, Hamburg, Germany. The basic design parameters

of the storage ring are an energy of 6 GeV and a current of 100 mA. The source of X-rays for HEMS was a 2 m long standard PETRA undulator. To select the radiation with a wavelength of λ = 0.1424 Å, an indirectly water cooled single bounce monochromator with a Si(220) Laue crystal was used [16,17]. The experiments were carried out in transmission Debye–Scherrer geometry and the distance between sample and detector was 1230 mm. The diffraction patterns were collected with a 2D-area PerkinElmer detector (Santa Clara, CA, USA).

The direct piezoelectric measurements were performed using a dynamic method. The measurement setup is a modified form of the one from Fukada and Yasuda [2]. This in-house setup consists of a metallic framework, which fixed the sample to be examined between two insulating corundum plates attached to a Piezo-Actuator (PA) type PICMA P-888.31, PI Ceramics, Lederhose, Germany, and frame. Using a RIGOL DG4062 function generator, Beijing, China, a sine voltage of 20 V was applied to the PA and converted into a dynamic mechanical load to the sample which was excited to oscillate at a frequency of 10 Hz. The alternating voltage produced by the sample was collected using an MMF M68D1 charge amplifier, Radebeul, Germany, with a gain of 1000 mV/pC. The data were collected with the help of PicoScope 6, Pico Technology, St. Neots, UK. This PicoScope was connected to a charge amplifier. First, a Non-Piezoelectric Material (NPM) was tested to interpret the maximum noise generated by the setup. Afterwards, pure and doped $CaTiO_3$ were investigated.

3. Results and Discussion

Figure 1 shows the EDX elemental mapping of the Mg and Fe doped $CaTiO_3$ samples, and the determined atomic fraction (at.%) of elements are presented in Table 1 together with pure $CaTiO_3$. In pure $CaTiO_3$, O, Ca and Ti are only present, but in doped samples, few at.% of Mg and Fe are also detected (Table 1). Additionally, a nearly homogenous distribution of these elements is found in the doped samples after SPS, with a strong reduction of large elemental segregation at the length scale of Figure 1. Carbon is also present in all samples (Table 1) which is caused by the sample's preparation for EDX experiments.

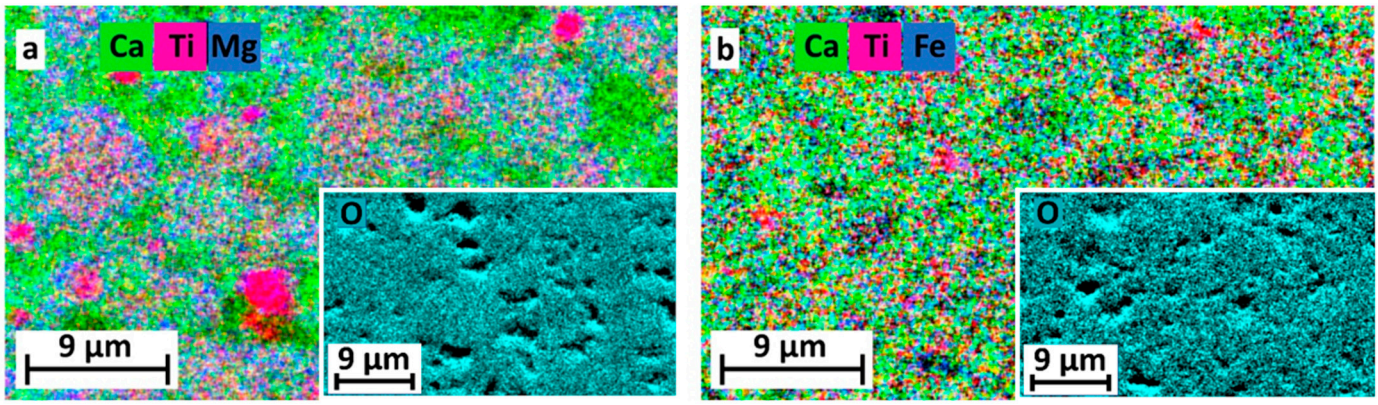

Figure 1. Elemental maps for the elements of the (**a**) Mg and (**b**) Fe doped $CaTiO_3$. (See web version for colors).

Table 1. Determined atomic fraction (at.%) of elements in the pure, Mg and Fe doped $CaTiO_3$. The standard deviation of each measurement is also presented.

$CaTiO_3$	Composition (at.%)					
	O	Ca	Ti	Mg	Fe	C
Pure	57 ± 5	16 ± 1	19 ± 1	–	–	8 ± 1
Mg doped	57 ± 5	15 ± 1	18 ± 1	2 ± 0	–	8 ± 1
Fe doped	56 ± 5	14 ± 1	17 ± 1	–	2 ± 0	10 ± 1

HEXRD patterns were integrated into 5° azimuthal steps and then all patterns were refined by Rietveld refinement [18] using the MAUD program v.2.94. (written by Luca Lutterotti, University of Trento, Italy [19,20]. It can be seen in Figure 2a that in all diffraction patterns, the main orthorhombic (pbnm) phase of nanostructured $CaTiO_3$ is present and their crystallite sizes (CS) are presented in Table 1. Small amounts of $MgTiO_3$ and $MgTi_2O_5$ phases were found in the Mg doped sample. However, in the Fe doped sample, only an additional Fe_2TiO_5 phase was present. The weight fractions of the corresponding phases are also presented in Table 2. Moreover, significant changes in the lattice parameters of $CaTiO_3$ orthorhombic phase of the doped samples are observed compared to the pure $CaTiO_3$ (see supplementary). It could be an indication of the replacement of doped cations, i.e., Mg and Fe by Ca cations, in $CaTiO_3$ crystal structure [21].

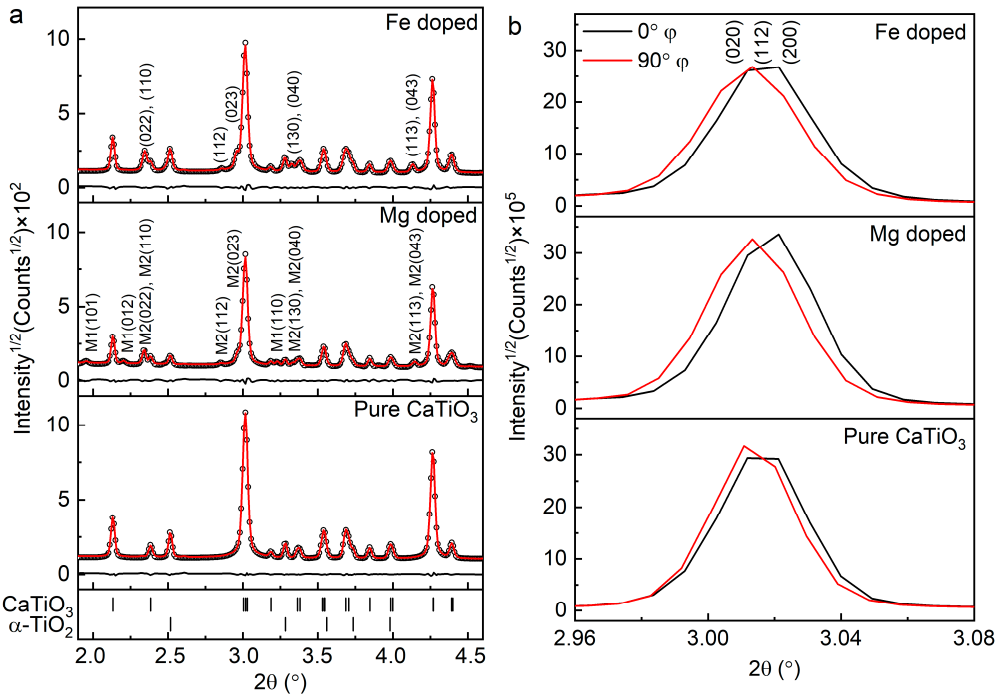

Figure 2. High Energy X-ray Diffraction (HEXRD) patterns of the pure, Mg and Fe doped $CaTiO_3$. The experimental pattern (black dots), the fitted pattern (red line) and the differential pattern (black line) are presented. Furthermore, Bragg positions of $CaTiO_3$ and α-TiO_2 phases are shown and main peaks of $MgTiO_3$ (M1), $MgTi_2O_5$ (M2) and Fe_2TiO_5, are labelled by corresponding Miller indices (**a**). Main peaks of $CaTiO_3$ phases of the pure, Mg and Fe doped samples at 0° and 90° azimuthal sectors. The peak is labeled by corresponding Miller indices (**b**). (See web version for colors).

Besides the integration of HEXRD patterns of whole Debye–Scherrer rings, the rings were also partially integrated into every 85° azimuthal step with a step width of 5° (see supplementary). In Figure 2b, the main peaks of orthorhombic phase of $CaTiO_3$ are presented with Miller indices (020), (112) and (200) at 0° and 90° azimuthal sectors. It is noticeable that the main peak position of pure $CaTiO_3$ at 90° azimuthal sector is shifted from 0° azimuthal sector. This peak shift is due to the lattice distortions influenced by SPS [22]. Furthermore, the peak position in Mg and Fe doped samples are shifted even more compared to pure $CaTiO_3$ indicating further lattice distortions as a result of doping elements. These lattice distortions and strains in the host lattice are due to cations replacement at the A site of perovskite and have also been observed previously [12,21].

To look over into more detail on the crystal structures of pure and doped samples, the lattice strains (ε) were investigated as a function of azimuthal sectors. For that purpose, the lattice parameters at the individual azimuthal sectors, i.e., 0°, 90°, 180° and 270°, were

determined and extracted by Rietveld refinement [18], and afterwards calculated with the help of Equation (1) [11]:

$$\varepsilon = (q - q_o)/q_o \quad (1)$$

where q represents lattice parameter values at azimuthal sectors when they are considered as an initial point, for example 0°, 90°, 180° and 270° and q_o represents lattice parameter values at azimuthal sectors when they are considered as a final point, for example 90°, 180°, 270° and 0°.

Figure 3 shows the lattice strain of lattice parameters *a*, *b* and *c* of main orthorhombic $CaTiO_3$ phase as a function of initial to final azimuthal sectors. In the pure $CaTiO_3$ sample, maximum lattice strain due to structural distortions (caused by defects) is observed in the lattice parameter *c*, and lattice strain in lattice parameters *a* and *b* is also present. This lattice strain is influenced by SPS, as reported in [11]. These azimuthal sectors dependent lattice strain in lattice parameters show that the Debye–Scherrer rings are elliptical but not circular in shape which is caused by structural distortions. Hence, electric dipole moments were generated because of the shift of positive and negative charges and resulted in the pseudo-piezoelectric effect [11], whereas in the Mg and Fe doped $CaTiO_3$, maximum lattice strain is observed not only in the lattice parameter *c*, but also in *b*. The magnitude of lattice strain for *a* remains approximately constant compared to pure $CaTiO_3$. It could be interpreted as stronger structural distortions (more elliptical Debye–Scherrer rings) and more defects in doped samples. For example, defects can be further influenced by the replacement of Ca to Mg or Fe cations which led to a change in the distortion of the $CaTiO_3$ crystal structure and may strengthen the generated electric dipole moments. These increased crystal distortions due to cations replacements should also influence the piezoelectric behavior and tune the strength of the piezoelectric effect.

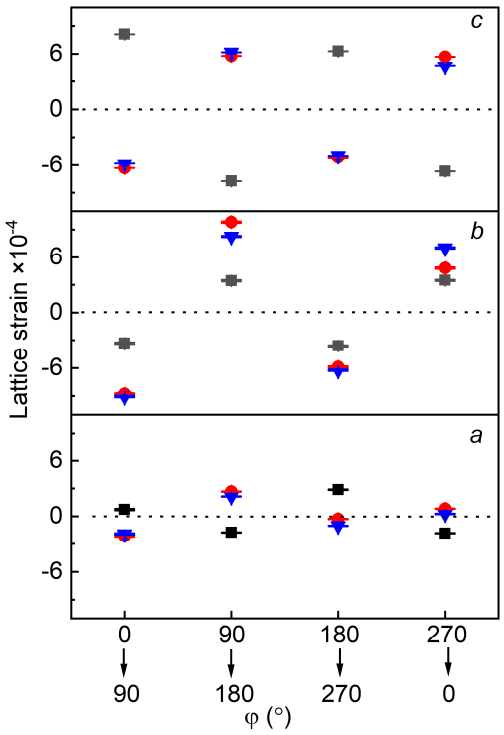

Figure 3. Lattice strain of lattice parameters *a*, *b* and *c* of main orthorhombic $CaTiO_3$ phases of the pure (black color), Mg (blue color) and Fe doped (red color) samples vs azimuthal sector. (See web version for colors).

Table 2. Determined crystallite sizes (CS), weight fractions (wt.%) of the contributing phases, and maximal charge produced by the pure, Mg and Fe doped $CaTiO_3$. The error of each measurement is also presented.

$CaTiO_3$	CS (nm)	Phases (wt.%)					Q (pC)
	$CaTiO_3$	$CaTiO_3$	α-TiO_2	Fe_2TiO_5	$MgTiO_3$	$MgTi_2O_5$	
Pure	219 ± 7	94.8 ± 0.5	5.1 ± 0.3	–	–	–	2.1 ± 0.3
Mg doped	175 ± 8	86.2 ± 0.2	4.7 ± 0.4	–	4.8 ± 0.3	4.2 ± 0.2	2.9 ± 0.1
Fe doped	163 ± 4	89.3 ± 0.4	5.2 ± 0.1	5.4 ± 0.2	–	–	3.6 ± 0.2

Figure 4 shows the responses of NPM and all sintered samples measured by the direct piezoelectric effect. The alternating output voltages generated by the pure, Mg and Fe doped $CaTiO_3$ can be seen. Furthermore, the input voltage represents the voltage which was applied for the oscillation of PA. It appears that NPM (V_{NPM}) produced a small alternating output voltage. This voltage represents the maximum noise generated by the experimental setup. It is conspicuous that the alternating output voltage (V_{CaTiO_3}) of the pure $CaTiO_3$ is significantly larger than the maximal noise of the setup. A further increase in V_{CaTiO_3} of the Mg doped sample is observed, and V_{CaTiO_3} of the Fe doped sample is even larger. It indicates the enhanced electric dipole strength of doped samples possibly caused by the different ionization states and radii of replaced Mg and Fe cations, and their influence on the increased structural distortions [23]. As a result, it also increases the pseudo-piezoelectric strength. L.H. Oliveira et al. also reported structural distortions as a function of Mg doping which was associated to the different ionic radii of cations and their repulsion in the A site of the perovskite structure [21]. It could also be possible that the small quantity of additional phases in doped samples slightly influenced the piezoelectric behavior. To calculate the maximal charge (Q) produced by all samples using the direct piezoelectric effect, equation 2 was used [11] and the values are shown in Table 2. Considering the increase in the pseudo-piezoelectric strength, it would be interesting to study the influence of additional phases, dependence of the fraction of doping elements in $CaTiO_3$ and their crystallite sizes for further application as a bone scaffold material. Additionally, the pseudo-piezoelectric response of the material can be tuned by doping giving the opportunity to study its impact in bone tissue engineering.

$$Q_{CaTiO_3} = V_{CaTiO_3}/\text{Gain} - V_{NPM}/\text{Gain} \quad (2)$$

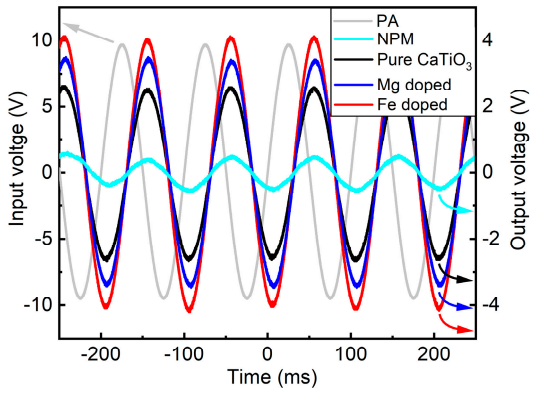

Figure 4. Time dependent voltage measurement of the NPM as well as pure, Mg and Fe doped $CaTiO_3$ though dynamic method. Moreover, the input voltage of the PA is shown. (See web version for colors).

4. Conclusions

In this study, pure, Mg and Fe doped $CaTiO_3$ were synthesized by sol-gel method and SPS and pseudo-piezoelectric strength was successfully tuned by doping of Mg and Fe in

$CaTiO_3$. The EDX-mapping showed the homogenous distribution of doping elements in sintered samples. The significant changes in lattice parameters of orthorhombic $CaTiO_3$ phase in pure and doped samples were observed. The doping of nanostructured $CaTiO_3$ increased the strain and defects in the structure of $CaTiO_3$ compared to the pure sample. Hence, an increase in pseudo-piezoelectric response is also observed in doped $CaTiO_3$. This effect was determined using the direct piezoelectric method. The produced charge in Mg doped sample was larger than pure $CaTiO_3$ and it was even more in Fe doped $CaTiO_3$. This tuning of pseudo-piezoelectric behavior provides the possibility of studying the bone response on a different pseudo-piezoelectric strength of scaffold material and to be engineered accordingly. This investigation can be extended to studying additional phases and whether they show piezoelectric behavior or not, as well as different fraction of doping elements in $CaTiO_3$ and their influence on piezoelectric behavior for further application as a bone scaffold material.

Supplementary Materials: The following are available online at https://www.mdpi.com/1996-1944/14/6/1495/s1, Figure S1: Lattice parameters of orthorhombic phase of the pure, Mg and Fe doped $CaTiO_3$, Figure S2: The 2D diffraction image shows Debye-Scherrer rings collected from HEXRD experiment. The azimuthal sectors at 0°, 90°, 180° and 270° are presented with red areas.

Author Contributions: Conceptualization, A.R., K.W., W.B. and E.B.; methodology, A.R.; validation, A.R., K.W., W.B. and E.B.; formal analysis, A.R.; investigation, A.R., K.W., W.B., H.S., N.S., A.S.; data curation, A.R.; writing—original draft preparation, A.R.; writing—review and editing, A.R., K.W., H.S. and E.B.; visualization, A.R., K.W. and W.B.; supervision, E.B.; funding acquisition, E.B. All authors have read and agreed to the published version of the manuscript.

Funding: This work was supported by the DFG Graduate School *welisa* (project no. 1506).

Institutional Review Board Statement: Not applicable.

Informed Consent Statement: Not applicable.

Data Availability Statement: The data presented in this study are available on request from the corresponding author.

Conflicts of Interest: The Authors declare no conflict of interest. The funders had no role in the design of the study; in the collection, analyses, or interpretation of data; in the writing of the manuscript, or in the decision to publish the results.

References

1. Bassett, C.A.L. Electrical effects in bone. *Sci. Am.* **1965**, *213*, 18–25. [CrossRef]
2. Fukada, E.; Yasuda, I. On the piezoelectric effect of bone. *J. Phys. Soc. Jpn.* **1957**, *12*, 1158–1162. [CrossRef]
3. Rajabi, A.H.; Jaffe, M.; Arinzeh, T.L. Piezoelectric materials for tissue regeneration: A review. *Acta Biomater.* **2015**, *24*, 12–23. [CrossRef] [PubMed]
4. Jacob, J.; More, N.; Kalia, K.; Kapusetti, G. Piezoelectric smart biomaterials for bone and cartilage tissue engineering. *Inflamm. Regen.* **2018**, *38*, 1–11. [CrossRef]
5. Khare, D.; Basu, B.; Dubey, A.K. Electrical stimulation and piezoelectric biomaterials for bone tissue engineering applications. *Biomaterials* **2020**, *258*, 120280.
6. Chen, W.P.; Chan, H.L.W.; Yiu, F.C.H.; Ng, K.M.W.; Liu, P.C.K. Water-induced degradation in lead zirconate titanate piezoelectric ceramics. *Appl. Phys. Lett.* **2002**, *80*, 3587–3589. [CrossRef]
7. Baxter, F.R.; Bowen, C.R.; Turner, I.G.; Dent, A.C.E. Electrically active bioceramics: A review of interfacial responses. *Ann. Biomed. Eng.* **2010**, *38*, 2079–2092. [CrossRef]
8. Webster, T.J.; Ergun, C.; Doremus, R.H.; Lanford, W.A. Increased osteoblast adhesion on titanium-coated hydroxylapatite that forms $CaTiO_3$. *J. Biomed. Mater. Res. Part A Off. J. Soc. Biomater. Jpn. Soc. Biomater. Aust. Soc. Biomater. Korean Soc. Biomater.* **2003**, *67*, 975–980. [CrossRef] [PubMed]
9. Ohtsu, N.; Sato, K.; Saito, K.; Asami, K.; Hanawa, T. Calcium phosphates formation on $CaTiO_3$ coated titanium. *J. Mater. Sci. Mater. Med.* **2007**, *18*, 1009–1016. [CrossRef]
10. Hamada, K.; Kon, M.; Hanawa, T.; Yokoyama, K.; Miyamoto, Y.; Asaoka, K. Hydrothermal modification of titanium surface in calcium solutions. *Biomaterials* **2002**, *23*, 2265–2272. [CrossRef]
11. Riaz, A.; Witte, K.; Bodnar, W.; Hantusch, M.; Schell, N.; Springer, A.; Burkel, E. Structural changes and pseudo-piezoelectric behaviour of field assisted sintered calcium titanate. *Materialia* **2021**, *15*, 100998. [CrossRef]

12. Wang, X.; Song, C.; Li, D.; Geng, K.; Zeng, F.; Pan, F. The influence of different doping elements on microstructure, piezoelectric coefficient and resistivity of sputtered ZnO film. *Appl. Surf. Sci.* **2006**, *253*, 1639–1643. [CrossRef]
13. Balakrishnan, S.; Padmanabhan, V.P.; Kulandaivelu, R.; Nellaiappan, T.S.N.; Sagadevan, S.; Paiman, S.; Mohammad, F.; Al-Lohedan, H.A.; Obulapuram, P.K.; Oh, W.C. Influence of iron doping towards the physicochemical and biological characteristics of hydroxyapatite. *Ceram. Int.* **2021**, *47*, 5061–5070. [CrossRef]
14. Prabhu, M.; Kavitha, K.; Manivasakan, P.; Rajendran, V.; Kulandaivelu, P. Synthesis, characterization and biological response of magnesium-substituted nanobioactive glass particles for biomedical applications. *Ceram. Int.* **2013**, *39*, 1683–1694. [CrossRef]
15. Chandra, U. *Recent Applications in Sol-Gel Synthesis*; BoD–Books on Demand: Norderstedt, Germany, 2017.
16. Schell, N.; King, A.; Beckmann, F.; Ruhnau, H.U.; Kirchhof, R.; Kiehn, R.; Müller, M.; Schreyer, A. The high energy materials science beamline (HEMS) at PETRA III. *AIP Conf. Proc.* **2010**. [CrossRef]
17. Schell, N.; King, A.; Beckmann, F.; Fischer, T.; Müller, M.; Schreyer, A. The high energy materials science beamline (HEMS) at PETRA III. *Mater. Sci. Forum* **2014**, *772*, 57–61. [CrossRef]
18. Rietveld, H. A profile refinement method for nuclear and magnetic structures. *J. Appl. Cryst.* **1969**, *2*, 65–71. [CrossRef]
19. Lutterotti, L.; Matthies, S.; Wenk, H.R.; Schultz, A.S.; Richardson, J.W., Jr. Combined texture and structure analysis of deformed limestone from time-of-flight neutron diffraction spectra. *J. Appl. Phys.* **1997**, *81*, 594–600. [CrossRef]
20. Lutterotti, L.; Bortolotti, M.; Ischia, G.; Lonardelli, I.; Wenk, H.R. Rietveld texture analysis from diffraction images. *Z. Kristallogr. Suppl.* **2007**, *26*, 125–130. [CrossRef]
21. Oliveira, L.H.; Savioli, J.; De Moura, A.P.; Nogueira, I.C.; Li, M.S.; Longo, E.; Varela, J.A.; Rosa, I.L. Investigation of structural and optical properties of $CaTiO_3$ powders doped with Mg^{2+} and Eu^{3+} ions. *J. Alloys Compd.* **2015**, *647*, 265–275. [CrossRef]
22. Riaz, A.; Witte, K.; Bodnar, W.; Burkel, E. Pseudo-piezoelectricity in calcium titanate–towards novel implant materials. *Scr. Mater.* **2020**, *188*, 274–278. [CrossRef]
23. Kour, P.; Pradhan, S.; Kumar, P.; Sinha, S.; Kar, M. Study of Ferroelectric and Piezoelectric Properties on Ca Doped PZT Ceramics. *Mater. Today Proc.* **2017**, *4*, 5727–5733. [CrossRef]